



## Unsupervised Sorting of Retinal Vessels Using Locally Consistent Gaussian Mixtures

Relan, D.; Relan, Rishi

*Published in:*  
Computer Methods and Programs in Biomedicine

*Link to article, DOI:*  
[10.1016/j.cmpb.2020.105894](https://doi.org/10.1016/j.cmpb.2020.105894)

*Publication date:*  
2021

*Document Version*  
Peer reviewed version

[Link back to DTU Orbit](#)

*Citation (APA):*  
Relan, D., & Relan, R. (2021). Unsupervised Sorting of Retinal Vessels Using Locally Consistent Gaussian Mixtures. *Computer Methods and Programs in Biomedicine*, 199, Article 105894. <https://doi.org/10.1016/j.cmpb.2020.105894>

---

### General rights

Copyright and moral rights for the publications made accessible in the public portal are retained by the authors and/or other copyright owners and it is a condition of accessing publications that users recognise and abide by the legal requirements associated with these rights.

- Users may download and print one copy of any publication from the public portal for the purpose of private study or research.
- You may not further distribute the material or use it for any profit-making activity or commercial gain
- You may freely distribute the URL identifying the publication in the public portal

If you believe that this document breaches copyright please contact us providing details, and we will remove access to the work immediately and investigate your claim.

## Journal Pre-proof

### Unsupervised Sorting of Retinal Vessels Using Locally Consistent Gaussian Mixtures

D. Relan, R. Relan

PII: S0169-2607(20)31727-2  
DOI: <https://doi.org/10.1016/j.cmpb.2020.105894>  
Reference: COMM 105894



To appear in: *Computer Methods and Programs in Biomedicine*

Received date: 14 November 2019

Accepted date: 26 November 2020

Please cite this article as: D. Relan, R. Relan, Unsupervised Sorting of Retinal Vessels Using Locally Consistent Gaussian Mixtures, *Computer Methods and Programs in Biomedicine* (2020), doi: <https://doi.org/10.1016/j.cmpb.2020.105894>

This is a PDF file of an article that has undergone enhancements after acceptance, such as the addition of a cover page and metadata, and formatting for readability, but it is not yet the definitive version of record. This version will undergo additional copyediting, typesetting and review before it is published in its final form, but we are providing this version to give early visibility of the article. Please note that, during the production process, errors may be discovered which could affect the content, and all legal disclaimers that apply to the journal pertain.

© 2020 Published by Elsevier B.V.

**Highlights**

- A four-step novel unsupervised methodology for retinal vessels clustering for fundus camera images.
- Homomorphic filtering (HF) to pre-process the input image for non-uniform illumination and denoising.
- Unsupervised multi-scale line operator segmentation technique.
- Use of only three discriminant features.
- Locally consistent Gaussian mixture model (LCGMM) for unsupervised classification of retinal vessels.

Journal Pre-proof

# Unsupervised Sorting of Retinal Vessels Using Locally Consistent Gaussian Mixtures

D. Relan<sup>a,\*</sup>, R. Relan<sup>b,c</sup>

<sup>a</sup>Department of Computer Science, BML Munjal University, Gurgaon, India

<sup>b</sup>Department of Applied Mathematics and Computer Science (DTU Compute), Technical University of Denmark, Kongens Lyngby, Denmark

<sup>c</sup>Siemens Energy, Gurgaon, India

## Abstract

**Background and Objectives:** Retinal blood vessels classification into arterioles and venules is a major task for biomarker identification. Especially, clustering of retinal blood vessels is a challenging task due to factors affecting the images such as contrast variability, non-uniform illumination etc. Hence, a high performance automatic retinal vessel classification system is highly prized. In this paper, we propose a novel unsupervised methodology to classify retinal vessels extracted from fundus camera images into arterioles and venules.

**Methods:** The proposed method utilises the homomorphic filtering (HF) to preprocess the input image for non-uniform illumination and denoising. In the next step, an unsupervised multiscale line operator segmentation technique is used to segment the retinal vasculature before extracting the discriminating features. Finally, the *Locally Consistent Gaussian Mixture Model* (LCGMM) is utilised for unsupervised sorting of retinal vessels.

**Results:** The performance of the proposed unsupervised method was assessed using three publicly accessible databases: INSPIRE-AVR, VICAVER, and MESSIDOR. The proposed framework achieved 90.14%, 90.3% and 93.8% classification rate in zone B for the three datasets respectively.

**Conclusions:** The proposed clustering framework provided high classification rate as compared to conventional Gaussian mixture model using Expectation-Maximisation (GMM-EM) approach, thus have a great capability to enhance computer assisted diagnosis and research in field of biomarker discovery.

**Keywords:** Retinal imaging, Blood vessels, Classification, Homomorphic filtering, multiscale line operator, Locally Consistent Gaussian Mixture Model

## 1. Introduction

Retinal imaging is a non-invasive in-vivo assessment of the human body's micro-circulation. There is a mounting evidence that systemic diseases can affect the arterioles and venules differently. The quantitative structural analysis of the retinal vasculature aids risk assessment of pathological condition in the retinal as well as other vascular systems [1–7]. For example, retinal arterioles narrowing is related to long-term risk of hypertension [1, 4, 8, 9], whereas, larger retinal venular calibre is related to renal insufficiency in individuals with type-1 diabetes [10]. Similarly, arteriolar-to-venular diameter ratio (AVR) is well-established biomarker for stroke and cardiovascular diseases [1, 4, 8, 11].

The basic requirement for the biomarker discovery is to access large number of images in order to establish and achieve sufficient power while ascertaining the association between clinical trait of diseases and retinal measure. In addition, an essential component of any computerised systems for retinal vasculature characterisation is vessel classification system which can classify vessels into arterioles and venules automatically.

This helps in an automatic extraction of vital diagnostic indicators. Thus, there is a great emphasis in the research community to develop a high quality automatic system for retinal vasculature characterisation and identification of discriminative biomarkers.

Various attempts have been made in the literature to classify the retinal vessels into arterioles and venules using different classification approaches [12–22]. Broadly, the vessel classification can be achieved either in an unsupervised or supervised manner. The supervised approach of vessel characterisation requires a large number of manual grading of vessels into arterioles and venules to produce suitable training data which is a tedious task. Moreover, one needs to train the classifier every time for the analysis of a new dataset, which further impedes the process of biomarker discovery. Thus, the supervised approach does not seem to be a good solution.

Furthermore, retinal vessel classification methods proposed in the literature can be broadly categorised into feature-based and tree-based methods. The tree-based approach focuses on segmenting and separating the retinal vessels into artery and venous trees based on the graph information e.g. at vessel crossings the two involved vessels are of different kind [23–25]. One of the major drawbacks of many complicated graph-based methods include the requirement of initial labels. Moreover, a

\*Corresponding author

Email addresses: devanjali\_relan@ed-alumni.net (D. Relan), risre@dtu.dk, rishi\_relan@siemens.com (R. Relan)

single false label propagates along the vessels and leads to misclassification of entire vessel tree [20, 23]. This becomes more pronounced in the region of low contrast e.g. especially in the peripheral regions.

On the contrary, the feature-based methods rely on discriminating vessel types based on colour, and geometric features [12, 26]. They rely on the fact that the arterioles are usually thinner as well as brighter than the venules and they typically alternate before branching out the optic disc (OD). In the literature, many frameworks to identify vessel types based on different discriminating features with different supervised [12, 18–21, 27–30] and unsupervised [13, 15–17] classification algorithms have been proposed.

The indicators of the quality of images such as resolution, contrast and background also affect the classification performance of such feature based automatic image analysis systems. This is due to the difficulty in extracting the robust discriminative features from the poor quality images. Therefore, preprocessing of images also plays a vital role in the retinal vessel classification.

In recent times, due to the democratisation of the open-source deep learning frameworks various methodologies for retinal vessel segmentation and classification based on deep learning networks have been reported in the literature [35–42]. For example, in a recent paper [32], the authors proposed a supervised framework using a convolutional neural network (CNN) to simultaneously segment and classify the retinal vessels. The authors tested different versions of the methods on DRIVE and MESSIDOR datasets. The best performance of the proposed algorithm was obtained with CNN and the metric of Likelihood score propagation (LSP). This version resulted in a classification rate of 85% for the vessels whose diameter was between 2 and 4 pixels whereas the classification rate obtained was 98.3% for the vessels whose diameter was greater than 4 pixels. Similarly, the authors in [35] trained a CNN architecture containing six learned layers to classify the retinal images. They tested their method on UK Biobank dataset and achieved the classification accuracy of 86.97% (pixel classification rate). The same deep learning network architecture when retrained on the DRIVE dataset resulted in 91.99%. It should be emphasised that the achieved high classification rates reported using the deep learning networks are in a supervised environment.

The Gaussian mixture model (GMM) based unsupervised classification method has been proposed previously in the literature [43]. The GMM based method assumes that the probability distribution generating the data is supported in the Euclidean space [44]. The general GMM might not attain an optimal result in case the data resides on a submanifold. Therefore, due to the above mentioned issues with the existing methods, in this paper, we propose to use the Locally Consistent Gaussian Mixture Model (LCGMM) [45] which considers the manifold structure for unsupervised classification of vessels into arterioles and venules. In case the data points are near to a submanifold of the ambient space, LCGMM incorporates a regularizer directly into the objective function of GMM after constructing the nearest neighbour graph and adopting *Kullback-Leibler Divergence* as the distance measurement.

In this paper, we utilise three publicly available datasets namely the INSPIRE-AVR (Iowa Normative Set for Processing Images of the Retina), VICAVR (VARPA Images for the Computation of the Arterio/Venular Ratio) and MESSIDOR (Methods to Evaluate Segmentation and Indexing Techniques in the field of Retinal Ophthalmology) dataset for evaluating the performance of the proposed system. The most relevant and important contributions available in the literature proposing different retinal vessel classification methods using discriminating features on the above mentioned datasets especially related to this paper are reported in Table 1. The four step methodology for unsupervised retinal vessel classification and the main contributions of the paper as briefly stated below:

- First a preprocessing step for illumination correction of the images using the homomorphic filter (HF) is proposed [46, 47]. The advantage of HF is that it helps in preserving the regions with sharp contrasts, for instance the regions with multiplicative noise (whose intensity varies with image intensity). Furthermore for denoising and enhancing the image quality at the same time, homomorphic filtering is an optimal choice [46, 47].
- In the second step, the retinal vessel segmentation is performed using an unsupervised multiscale line operator [48, 49]. For unsupervised segmentation, the multiscale line operator is an optimal choice to avoid false positives while differentiating between close vessels and vessels with central reflex [50].
- After the segmentation step, the centerline pixels and vessel edges are extracted using a simple canny edge detector [51] and the images are then used for feature extraction.
- Finally, based on the set of extracted features an unsupervised arteriole-venule (a-v) classification is performed using the LCGMM [45].

In our previous work, we performed unsupervised vessel classification [43]. The present framework is different as compared to previous setting such as, illumination correction was performed prior to feature extraction for the vessel classification. Moreover, in previous work, the centerline pixels were extracted by tracking the vessel between manually marked points on the vessels whereas in this paper, vessel segmentation was performed to extract the centerline pixels automatically. Furthermore, the vessels were selected automatically in this work whereas in previous work [43] the vessels were selected manually.

The paper is organised as follows. Section 2 provides the details of the material utilised during this study, whereas Section 3 introduces various methods and steps used in the proposed framework. Section 4 describes the LCGMM algorithm. Section 5 gives the main performance metrics used in this paper. Section 6 reports the results obtained. Section 7 presents a discussion followed by the conclusions in Section 8.

Table 1: Literature survey on retinal vessel classification on INSPIRE-AVR, VICA VR and MESSIDOR dataset

Author [Reference]	Classifier	Dataset	Zone	Result
Dashtbozorg et al. [20]	LDA*, QDA <sup>†</sup> & kNN <sup>‡</sup> , FS <sup>°</sup> : SFFS**	INSPIRE-AVR, DRIVE & VICA VR	Whole Image	LDA (best performed): 88.3%, 87.4% & 89.8% respt.
M. Niemeijer et al. [27]	LDA*, QDA <sup>†</sup> , SVM*, kNN <sup>‡</sup> , FS <sup>°</sup> : SFFM** & wrapper based	INSPIRE-AVR	zone B	Best result:LDA ROC: 0.84
Vijayakumar et al. [29]	SVM + Other classifiers, Feature selection: Random forest	VICA VR	Whole Image; Major vessels	Best Result with SVM: 92.4%
Vazquez et al. [31]	K-mean and tracking method	VICA VR	Several circumferences on an Image	87.68%
Fantin Girard et al. [32]	CNN and graph propagation	MESSIDOR	Whole Image vessels with diameter between 2 to 4 pixels and greater then 4 pixel	Best result: 85.1% & 98.3% respt.
D. Relan et al. [33]	SMIC***	INSPIRE-AVR, DRIVE	zone B	87.6% & 86.2% respt.
D. Relan et al. [34]	SMIC***	INSPIRE-AVR, DRIVE	zone B	88.9% & 93.2% respt.

\* LDA: Linear discriminant analysis, ‡ kNN: k-nearest neighbours, \*\* SFFM: Sequential forward floating method, ★ SVM: Support vector machine, ● FFS: Forward feature selection, ◊BP: Bypass connections, \*\*LSP:Likelihood score propagation, \* \* \*SMIC: Squared-loss mutual information, °CNN: Convolutional Neural Networks, † QDA: Quadratic Discriminant Analysis.

## 2. Material

In this paper, three publicly available fundus camera image datasets namely: INSPIRE-AVR, VICA VR, and MESSIDOR are used to assess the performance of the proposed unsupervised vessel sorting method. The details of the datasets are provided below:

1. INSPIRE-AVR: It contains 40 optic disc-centred colour fundus camera images [27]. Details about image acquisition such as camera system and Field of view (FoV) are not given in [27]. To access the performance of the proposed vessel clustering method, 544 vessels were extracted automatically from zone B. The resolution of the images contained in this dataset is  $2392 \times 2048$  pixels.
2. VICA VR: The VICA VR database contains 58 optic disc-centred fundus camera images which were captured using a non-mydratic camera [31]. The spatial resolution of images is  $768 \times 584$ . The proposed methodology was tested on 732 vessels extracted from zone B of retinal images.

3. MESSIDOR: The images were obtained from non-mydratic 3CCD camera having a 45 degree field of view. We tested our method on 60 images from this dataset with 20 images each from the group of normal, retinopathy grade 1 and retinopathy grade 2. Each of the tested image has a resolution of  $2240 \times 1488$  pixels.

## 3. Methodology

The proposed unsupervised methodology contains a series of steps for classifying the vessels from the fundus camera images Figure1 shows the work-flow and the steps involved in the proposed methodology.

### 3.1. Image pre-processing

The quality of the image often gets affected by noise, non-uniform illumination, camera artefacts, obstruction from eye lashes, etc. during the image acquisition. The colour variability and luminosity effects the performance of the automatic

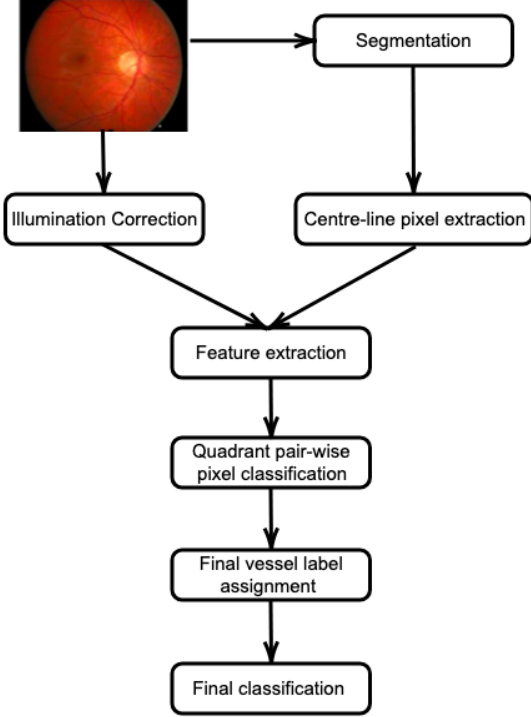


Figure 1: Flow chart describing the main steps in a-v classification utilising the discriminative features.

image analysis system. Thus, to classify vessels efficiently and accurately, it is essential to preprocess the image against this variability factors before the extraction of discriminating features. Literature provides several different image denoising or enhancement techniques that assume an additive noise model [52, 53], but few methods work with the multiplicative model.

Furthermore, the common reported linear filtering and smoothing techniques, such as averaging filters cannot account for a slow variation of the global illumination (like progressive shadowing effect) and enhance the image quality at the same time because the image composition is not often linear and therefore linear methods tend to be sub-optimal. One common technique for removing multiplicative noise is homomorphic filtering [46, 47]. Homomorphic filters work well on images taken under varying illumination conditions as well as with noise varying with intensities, such as fundus images [54, 55].

Thus, in the first step, homomorphic filtering is utilised to compensate for the background illumination in red and green channels and for noise reduction. The mathematical principle behind the homomorphic filtering is briefly described below.

### 3.1.1. Homomorphic Filtering

Illumination-Reflectance model of Homomorphic filtering [56, 57], is given by,

$$Im(k, l) = Rf(k, l) \times IL(k, l) \quad (1)$$

where  $Im(k, l)$  denotes the pixel in an image at each of the spatial positions  $(k, l)$ ,  $IL(k, l)$  stands for scene illumination (or luminance) and  $Rf(k, l)$  is the scene reflectance. This shows that

the pixel intensity at any image point is the product of the object's reflectance and illumination of the scene.

The main idea of the homomorphic filtering is to eliminate the illumination element  $IL(k, l)$  and to keep only the reflectance part  $Rf(k, l)$  to compensate for the non-uniform illumination. Illumination and reflectance are not detachable easily in time or spatial domain, but rather their approximate location might be found in the frequency domain. The fundamental difference to separate out the illumination component from the reflectance component is that illumination changes slowly over the image whereas reflectance changes abruptly at object edges. Furthermore, the illumination and the reflectance component combine multiplicatively, which can be made additive in log-domain by taking the logarithm of the image intensity. This operation makes it easier to separate the multiplicative components of the image linearly in the frequency domain. Thus, in homomorphic filtering, multiplicative components is first transformed into additive components using logarithmic function,

$$\ln(Im(k, l)) = \ln(Rf(k, l)) + \ln(IL(k, l)) \quad (2)$$

where,  $\ln$  represents the logarithmic operation. Thereafter, the Fast Fourier Transform (FFT) of the log-transformed image was performed such that,

$$\mathcal{F}(\ln(Im(k, l))) = \mathcal{F}(\ln(Rf(k, l))) + \mathcal{F}(\ln(IL(k, l))) \quad (3)$$

$$Im_f(u, v) = Rf_f(u, v) + IL_f(u, v) \quad (4)$$

where,  $\mathcal{F}$  represent the FFT operation.  $Im_f(u, v)$ ,  $Rf_f(u, v)$  and  $IL_f(u, v)$  represent the Fourier transformed image, reflectance and Illumination component respectively. Finally to eliminate the illumination part,  $IL(k, l)$  (low-frequency component), and preserving the reflectance part,  $Rf(k, l)$  (high-frequency component), a Gaussian high-pass filter in the log-domain is used. Next, applying a high-pass filter to the image yields,

$$FI(u, v) = Hpl(u, v) \times Im_f(u, v) \quad (5)$$

where,  $Hpl$  represents the high-pass filter and  $FI$  represents a filtered image in frequency domain. Once the illumination component  $IL(k, l)$  and the reflectance component  $Rf(k, l)$  are separated then, the inverse-FFT is computed in order to convert the frequency domain image back to the spatial domain.

$$n(k, l) = \mathcal{F}^{-1}(FI(u, v)) \quad (6)$$

where,  $\mathcal{F}^{-1}$  represent the inverse-FFT operation. Finally, to get the homomorphic filtered image, the exponential function is applied to invert the log-transform,

$$I_{new}(k, l) = \exp(n(k, l)) \quad (7)$$

where,  $\exp: z \mapsto e^z$  is the exponential function and  $I_{new}$  represents homomorphic filtered image. Figure 2 shows the original green channel image and illumination corrected image using homomorphic filtering from each dataset.

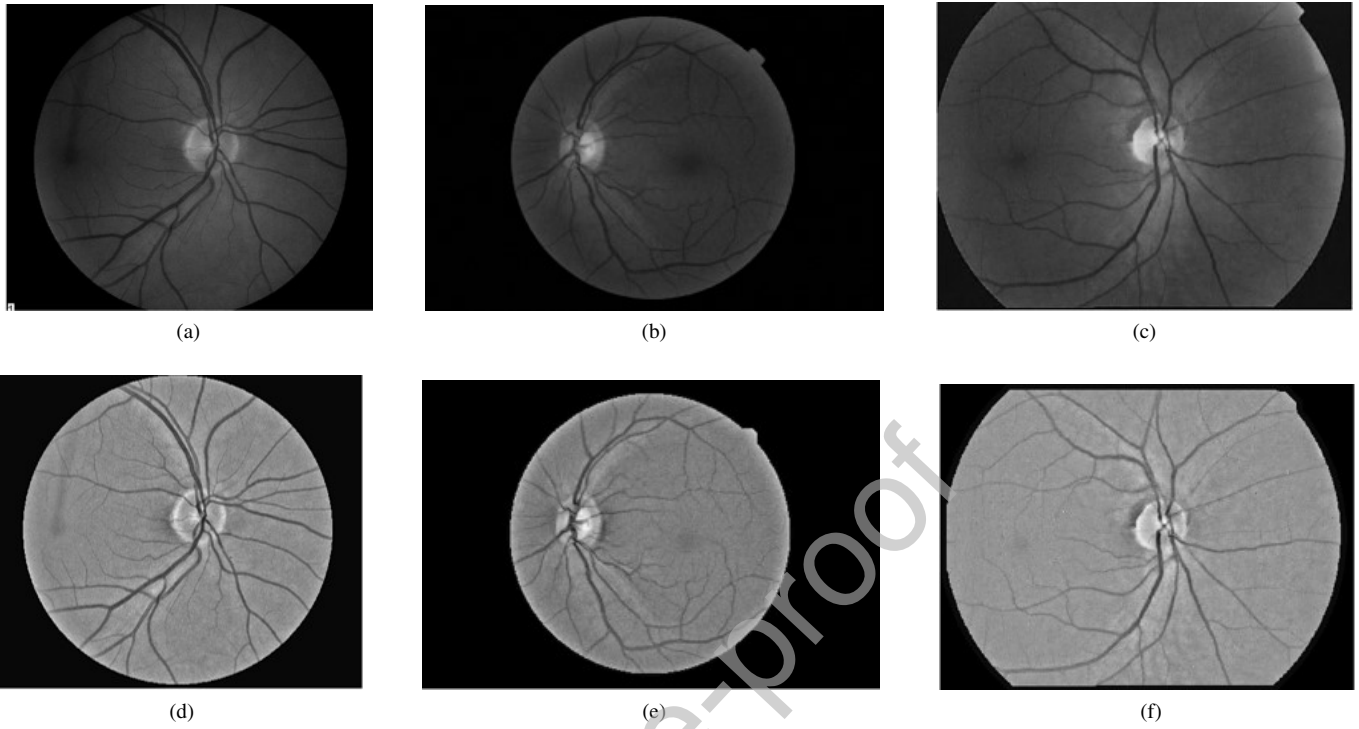


Figure 2: Figure showing the images before ((a), (b) and (c)) and after processing with homomorphic filtering ((d), (e) and (f)) using INSPIRE, MESSIDOR and VICAVER dataset images respectively.

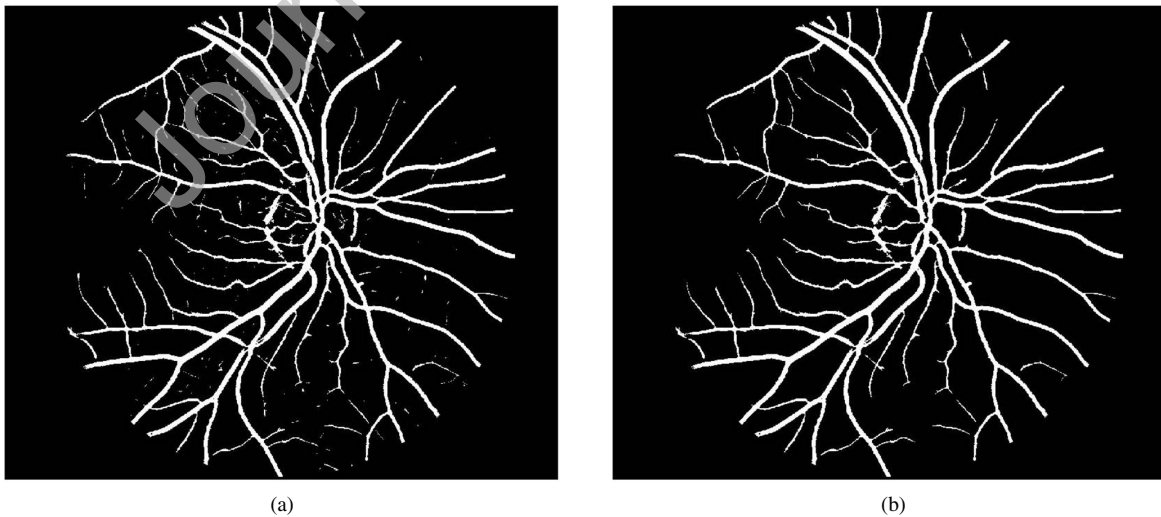
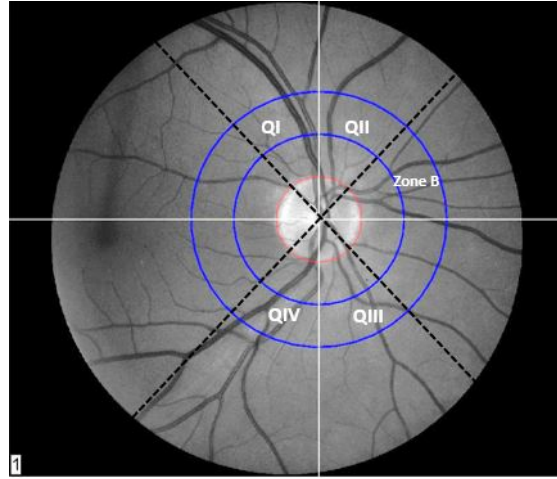
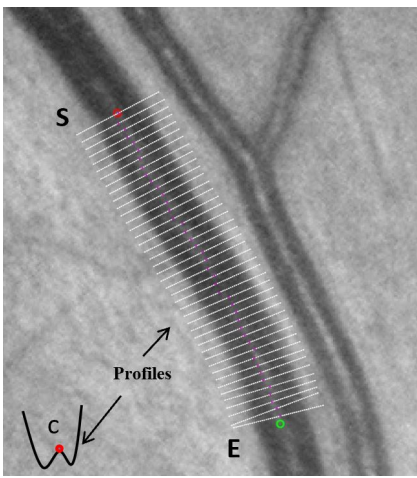


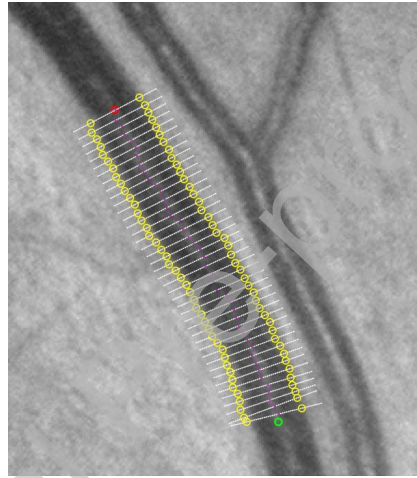
Figure 3: (a) Segmented image from INSPIRE dataset using multiscale line operator with  $W= 50$  and  $L= 3$  (b) Segmented image from INSPIRE dataset after removing all connected objects that have fewer than 400 pixels.



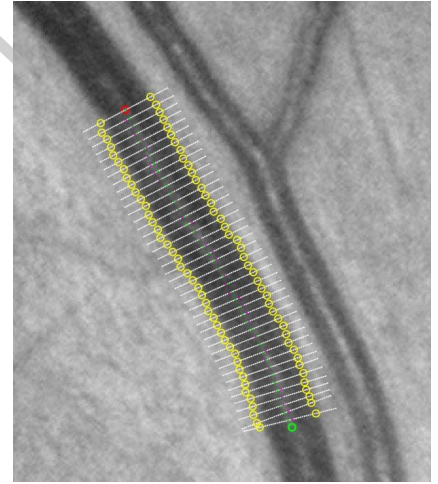
(a)



(b)



(c)



(d)

Figure 4: (a) Image showing zone B between two blue concentric lines. Image is divided into 4 different quadrants( QI, QII, QIII and QIV), indicated by white solid line passing through OD centre whereas when co-ordinates are rotated by  $45^\circ$  is represented by black dashed lines, (b) Image showing set of profiles located between start and end points represented by red and green points respectively, (c) Image showing edges extracted using canny edge detector from each of the profile. Edges are marked as yellow circles, and (d) Centerline pixels (indicated by green dots) were evaluated as midpoint between two corresponding edge points.

### 3.2. Unsupervised Vessel Segmentation and Centerline pixel extraction

An accurate vessel segmentation plays a key part in order to quantify various features associated with various systemic diseases such as the changes occur in vessel calibre, vessel tortuosity or branching angle due to hypertension [58–60], neo-vascularization which is an indicator of diabetic retinopathy [61, 62], arterio-venous nicking which is a precursor of stroke [63–65] etc.. In the past various attempts using both supervised and unsupervised techniques were made to segment the retinal vessels [66–70]. In this paper, in order to design an unsupervised framework, we utilize the unsupervised line operator technique for the segmentation of retinal images.

As the first step in the basic line operator technique for segmenting the input image into a binary image, the green channel was extracted [48–50]. Thereafter, the mean grey level  $I_{avg}^W$  is calculated along the lines passing through the pixels at different orientations inside the window of size  $W \times W$  pixels [48, 71]. The

basic line operator technique suffers from parameter adjusting issue i.e if the size of the scale selected for the line is smaller than the width of the vessels it will result in poor segmentation output [72]. Therefore, we used the multiscale approach so that none of the blood vessel pixels is ignored and to avoid the parameter adjusting problem [72]. The green channel was used to segment the image as it shows a good contrast between the vessel w.r.t. its background. We considered 12 lines of length  $W$  pixels with 12 different orientations. This setting provides the angular resolution of  $15^\circ$  which covers the whole window in 360 degrees [50]. The line with the largest value,  $I_{max}^W$ , is said to be 'winning line'. The *line strength / response* at any pixel is given by,

$$R_W = I_{max}^W - I_{avg}^W \quad (8)$$

The line response is considered maximum, if the winning line is aligned along the vessel and in case the overlap is partial, the line strength is considered to be lower. The parameter  $W$ ,

is taken as double the expected average width of the vessels in an image set [48–50]. Multiscale line detectors are based on generalising the basic line detector. In multiscale line detector the length of the aligned lines varies and the generalised form is given by:

$$R_W^L = I_{max}^L - I_{avg}^W \quad (9)$$

where  $1 \leq L \leq W$ .

**Remark 3.1.** We have chosen  $L = 3$  in our experiments. The experimental parameters,  $L$  and  $W$ , were selected based on the experiments performed by authors on three independent datasets namely the DRIVE, STARE, and REVIEW datasets [50] and cross validation experiment tests on few of the randomly selected images from the datasets used in this current paper. Based on the analysis on randomly selected images, we selected  $W = 50$  for the INSPIRE and MESSIDOR datasets and  $W = 16$  for VICAVER datasets.

After the segmentation step, the images were cleaned and all connected components (small objects) that have smaller than 400 pixels were removed from the binary images using *bwareopen* function in MATLAB. This setting worked well for images from both the datasets. Fig. 3 shows the segmented image using multiscale line operator before and after removing connected components. Finally, the following steps were involved in selecting vessels, inside the zone B,

1. **Find and remove all junctions:** In order to find a junction, first the binary or segmented image was skeletonized using *bwmorph* function in MATLAB. The function is based on an iterative scheme for the deletion of pixels [73]. Thereafter to separate the vessels from each other, all the junction points in an image were identified and deleted from skeletonized image [74].
2. **Select the major vessels:** In this step, to select the major vessels from all the detectable vessels, the properties for each vessel segments were measured using Matlab's *regionprops* function. Then, using *PixelList* property, we retained those vessels whose length is greater than or equal to *thresh*. The parameter *thresh* was set equal to 50 for INSPIRE and MESSIDOR images and 25 and VICAVER images. This parameter was selected based on the experiments conducted on randomly selected sets of images from each dataset. The main aim of the experiments was two-fold i.e. to search for the parameter value such that the maximum number of vessels are retained and very short vessels are removed.
3. **Finding centerline pixels and vessel width:** In this step, the Canny edge detector [51] was utilised to find the vessel edges. To do so, first the intensity profiles across the vessel were identified after every  $5^{th}$  pixel between the start ( $S$ ) and the end ( $E$ ) pixels (denoted by red and green colours respectively; See Fig. 4(b)). The  $S$  and  $E$  pixel points are the first and last pixel in the pixel list of the detected vessel during segmentation, found in previous step. In our previous work, these two points were placed manually on the

vessel [43]. Thereafter, the vessels were tracked between these two automatically selected start and end points. The tracking process between these two points is similar to one explained in our previous work [43].

During the tracking process the cross-sectional intensity profiles (indicated by dotted lines across the vessels in Fig. 4(b)) were found between start and end point at every  $5^{th}$  pixel. These profiles appears as an inverted bell shape (Gaussian); see Fig. 4(b). The point  $C$  (indicated in red) on the intensity profile gives the approximate vessel centre. This point can be established by finding and averaging two local minimum points on the vessel profile.

Thereafter, in order to find vessel edges (indicated by yellow circles) (see Fig. 4(c)), the canny edge detector [51] was applied on all detected intensity profiles. Lastly, the centerline pixels (showed by green dots in Fig. 4(d)) were detected at the midpoint of the edge points pair [43]. The distance between the two opposite edges was then stored as a width of the vessel. In this way, the vessel centerline pixels were obtained in all the four quadrants ( QI, QII, QIII and QIV) (See Fig. 4(a)).

4. **Vessel selection for classification:** Based on the width calculated by the canny edge detector, those vessels were selected whose width  $\geq 60\%$  of  $M_V$  where,  $M_V$  is the width of the thickest vessel among all vessels in a pair of adjacent quadrants. The 60% threshold criterion was arrived at experimentally. The experiments were also conducted using the 50% and the 70% criterion. The 50% criterion selects very thin confusing vessels whereas, the 70% criterion resulted in selection of lesser number of vessels. Therefore, the 60% criterion was found to be a reasonable choice in order to select the larger vessels containing a combination of medium to wider vessels. The main aim behind designing such a selection criterion is to robustly calculate the Arterio-Venous Ratio (AVR) (biomarker for various systemic disease). For the measurement of AVR, it is always advisable to select the good quality vessels since otherwise it is not possible, even for an ophthalmologist, to distinguish between arteries and veins [75]. In the subsequent step, the selected vessels participated for vessel classification.

### 3.3. Feature Extraction

In this step, to perform vessel classification only three features: the variance of red (VR), mean of red (MR) and green (MG), were extracted. These fixed colour features are widely reported in the literature and are considered to be some of the most discriminating and informative features for retinal vessel classification [13, 76, 77]. The features were extracted from the illuminated corrected channel/image around the circular neighbourhood of each centerline pixel. The diameter of this circular region of interest around the pixel is taken 60% of the average width of the vessel. The rationale behind this approach is to calculate the features always inside the selected vessel.

### 3.4. Vessel Classification

Finally, the LCGMM classifier (see Section 4 for the detailed explanation) was utilised to classify each vessel centerline pixel taken from two adjacent neighbourhood quadrant (i.e. quadrant pair: (QI, QII), (QII, QIII), (QIII, QIV) and (QIV, QI)). Thus, clustering process assign one label to each centerline pixel. As vessels in neighbouring quadrants participated twice in classification process therefore two labels were given to every centerline pixel. For example, the vessel in quadrant **QI** is classified twice as it belong to quadrant pair (**QI, QII**) and (**QIV, QI**).

After this, the quadrants were rotated (represented by black dashed lines; see Fig. 4(a)) and the vessel's centerline pixels belonging to adjacent rotated quadrant were again classified. This generates two additional labels to each centerline pixel. Thus, in this way all the centerline pixels were assigned four labels. Thereafter, the hard label was allotted to the centerline pixel depending upon the majority of soft labels of each type. Finally, the vessels were grouped as arteriole or venule depending on the highest number of hard labels of each type. The vessel was marked unclassified in case the votes were tied [43].

## 4. Locally Consistent Gaussian Mixture Model

In many applications, it is quite common that the data can be represented by a fewer data points than the actual dimension of the acquired data would suggest [78, 79]. In such cases, the general GMM might not be an ideal choice to represent the data since it does not take into account the geometrical information e.g. the generated data may be close to submanifold of the actual ambient space. Therefore in following section, we describe briefly the LCGMM method that efficiently incorporates the geometrical information of the probability distribution into learning a GMM. In the section below, firstly a very brief introduction to classic GMM is given thereafter the procedure to learn a LCGMM is described in details.

### 4.1. Background

The GMM is realised with a linear (weighted) mixture of various Gaussian components. Each Gaussian component act as a basis function, thus offering a comparatively richer class of density models than a single Gaussian [44]. Mathematically, a Gaussian mixture density function can be defined as:

$$P(M|\Omega) = \sum_{k=1}^K \pi_k p_k(m|\theta_k). \quad (10)$$

where  $M = (m_1, m_2, \dots, m_N)$  are the observations,  $\pi_k \geq 1$  can be viewed as positive weights on each individual Gaussian component and it satisfies the convex relation  $\sum_{k=1}^K \pi_k = 1$ . The parameter vector is represented by  $\Omega = (\pi_1, \dots, \pi_K, \theta_1, \dots, \theta_K)$ . Note that here each Gaussian density function  $p_k$  is parameterised by  $\theta_k$ , meaning that  $p_k(m|\theta_k) \sim \mathcal{N}(m|\mu_k, \Sigma_k)$ , where  $\mu_k$  is the mean and  $\Sigma_k$  is the covariance matrix of the component.

The Maximum-likelihood estimation (MLE) is commonly used to the set of optimal parameter  $\Omega$  given observations  $M$  such that  $P(M|\Omega)$  is maximised. For better numerical efficiency,

the optimisation is generally carried out in log-domain by introducing the log-likelihood function, which is defined as,

$$\mathcal{L} = \log P(M|\Omega) = \log \prod_{i=1}^N P(m_i|\Omega) \quad (11)$$

$$= \sum_{i=1}^N \log \sum_{k=1}^K \pi_k p_k(m_i|\Omega) \quad (12)$$

In the above expression, it is difficult to find a closed form expression for the ML optimal solution. By introducing the latent variable  $P(s|m)$  which represents the probability of observation  $m$  belonging to component  $s$ , the log-likelihood function can be formulated as [44]:

$$\mathcal{L} = \sum_{i=1}^N \sum_{k=1}^K P(c_k|m_i) \log \pi_k + \log \mathcal{N}(m_i|\mu_k, \Sigma_k) \quad (13)$$

The ML estimate for  $\Omega$  under the assumption that  $P(s|m)$  can now be obtained using the Expectation-Maximisation (EM) algorithm [80].

### 4.2. GMM and Locally Consistency

In general, for function learning from examples, it is assumed that the examples are generated according to a probability distribution  $P$  on  $M \times \mathbb{R}$  and the unlabelled examples  $m \in M$  are assumed to be drawn according to the marginal distribution  $P_M$  of  $P$ . The method presented in the section below exploits the connection between the marginal and conditional distributions under the following assumption [81]:

**Assumption 4.1.** Within some neighbouring samples, the conditional probability distribution  $P(s|m_i)$ , where  $s$  represents the clusters, are similar to a certain degree or in other words,  $P(s|m)$  varies smoothly along the geodetic surface in the intrinsic geometry of  $P_M$

**Remark 4.1.** This assumption is usually known as the *local consistency assumption* [82, 83], which is a central idea behind various kinds of algorithms including semi-supervised learning [81, 84] and dimensionality reduction [85] algorithms.

*Kullback-Leibler Divergence* (KL-Divergence) is one of the most common methods to measure the "similarity" (or "distance") between two probability distributions and is defined as,

$$\mathbb{D}(P_i(s)||P_j(s)) = \sum_s P_i(s) \log \frac{P_i(s)}{P_j(s)} \quad (14)$$

where,  $P_i(s)$  and  $P_j(s)$  are two probability distributions functions. Due to the asymmetry, it can be reformulated to evaluate the distance between two distributions  $P_i(s)$  and  $P_j(s)$  as follows,

$$\mathbb{D}_{ij} = \frac{1}{2} (\mathbb{D}(P_i(s)||P_j(s)) + \mathbb{D}(P_j(s)||P_i(s))) \quad (15)$$

It has been shown in the literature that the local geometric structure can be modelled through a nearest neighbour graph on a scatter of data points [85, 86]. Therefore, let us consider a graph

with  $N$  vertices, where each vertex in the graph corresponds to a data point and the edge weight matrix  $W$  defined as follows:

$$W_{ij} = \begin{cases} 1 & \text{if } m_i \in N_n(m_j) \text{ or } m_j \in N_n(m_i) \\ 0 & \text{otherwise} \end{cases}$$

where  $N_n(m_i)$  represents the data sets of  $n$  nearest neighbours of  $m_i$ . By letting  $P(s) = P(s|m_i)$ , with the weight matrix of the nearest neighbour graph as in (4.2), the smoothness of  $P_i(s|m)$  on the graph can be measured as described below:

$$\mathcal{R} = \sum_{i,j=1}^N \mathbb{D}_{ij} W_{ij} \quad (16)$$

$$= \frac{1}{2} \sum_{i,j=1}^N \mathbb{D}(P_i(s)||P_j(s)) + \mathbb{D}(P_j(s)||P_i(s)) W_{ij} \quad (17)$$

The smaller the value of  $\mathcal{R}$ , the smoother the  $P(s|m)$  is over the graph or in other words along the geodesics in the intrinsic pattern of the data [45].

#### 4.2.1. Likelihood function

The smoothness term described in the previous section can now be incorporated into the likelihood of original GMM as below,

$$\mathcal{L} = \mathcal{L} - \lambda \mathcal{R} \quad (18)$$

$$\propto \sum_{i=1}^N \log \sum_{k=1}^K \pi_k \mathcal{N}(m_i|\mu_k, \Sigma_k) \quad (19)$$

$$- \frac{\lambda}{2} \sum_{i,j=1}^N \mathbb{D}(P_i(s)||P_j(s)) + \mathbb{D}(P_j(s)||P_i(s)) W_{ij} \quad (20)$$

where  $P_i(s)$  represents the  $P(s|m_i)$  and  $\lambda$  is the regularisation parameter. As the local consistency is incorporated through a regularizer, therefore the method is termed as the Locally Consistent Gaussian Mixture Model (LCGMM) [45].

### 4.3. Model Fitting with EM

The parameter vector (latent variables) in the LCGMM method is denoted by  $\Omega = (\pi_1, \dots, \pi_K, (\mu_1, \Sigma_1), \dots, (\mu_K, \Sigma_K))$ . The ML estimate of  $\Omega$  can be calculated using the Expectation-Maximisation (EM) algorithm [80]. The EM algorithm involves two steps namely, 1) the E-step, i.e computing expected values for the latent variables and 2) The M-step, which uses the computed expected values of the variables to obtain the parameters which maximise the log likelihood. The above mentioned steps are repeated until a certain pre-specified stopping criterion is reached.

#### 4.3.1. E-step:

The computation of the posterior probabilities for the latent variables are  $P(s_k|m_i)$ , can be done by simple application of Bayes' rule [44]:

$$P(s_k|m_i) = P(s_k = 1|m_i) = \frac{\pi_k \mathcal{N}(m_i|\mu_k, \Sigma_k)}{\sum_{j=1}^K \pi_j \mathcal{N}(m_i|\mu_j, \Sigma_j)} \quad (21)$$

#### 4.3.2. M-step:

The expected complete data log-likelihood for LCGMM can then be obtained as follows [44]:

$$\begin{aligned} Q(\Omega) &= Q_1(\Omega) - Q_2(\Omega) \quad (22) \\ &= \sum_{i=1}^N \sum_{k=1}^K P(s_k|m_i) (\log \pi_k + \log \mathcal{N}(m_i|\mu_k, \Sigma_k)) \\ &\quad - \frac{1}{2} \sum_{i,j=1}^N (\mathbb{D}(P_i(s)||P_j(s)) + \mathbb{D}(P_j(s)||P_i(s))) W_{ij} \end{aligned}$$

It can be clearly seen in (22) that  $Q(\Omega)$  consists of two parts. The first part  $Q_1(\Omega)$  describes the expected complete data log-likelihood for LCGMM exactly similar to GMM in (13), whereas, the second part  $Q_2(\Omega)$  describes the *locally consistent regularizer* only involving the parameters  $\{\mu_k, \Sigma_k\}_{k=1}^K$ . The part of  $Q(\Omega)$  which is relevant to  $\{\mu_k, \Sigma_k\}_{k=1}^K$  can be described as [45]:

$$\tilde{Q}(\Omega) = \tilde{Q}_1(\Omega) - Q_2(\Omega) \quad (23)$$

where,

$$\tilde{Q}(\Omega) = \sum_{i=1}^N \sum_{k=1}^K P(s_k|m_i) \left( \frac{1}{2} \log(|\Sigma_k^{-1}|) - \frac{1}{2} (m_i - \mu_k)^T \Sigma_k^{-1} (m_i - \mu_k) \right) \quad (24)$$

The M-step re-estimation equation for  $\mu_k$  can be obtained by taking the derivative of (23) with respect to (w.r.t.)  $\mu_k$  and setting it to zero as below:

$$\mu_k = \frac{\sum_{i=1}^N m_i P(s_k|m_i)}{N_k} \quad (25)$$

$$- \frac{\lambda \sum_{i,j=1}^N (P(s_k|m_i) - P(s_k|m_j)) (m_i - m_j) W_{ij}}{2N_k} \quad (26)$$

where,  $N_k = \sum_{i=1}^N P(s_k|m_i)$ . By defining  $S_{i,k} = (m_i - \mu_k)(m_i - \mu_k)^T$ , we have:  $(m_i - \mu_k)^T \Sigma_k^{-1} (m_i - \mu_k) = \text{Tr}(S_{i,k} \Sigma_k^{-1}) = \text{Tr}(\Sigma_k^{-1} S_{i,k})$ , where  $\text{Tr}(\bullet)$  denotes the trace operator of a matrix. Now, (23) can be rewritten as:

$$\tilde{Q}_1(\Omega) = \frac{1}{2} \sum_{i=1}^N \sum_{k=1}^K P(s_k|m_i) (\log |\Sigma_k^{-1}| - \text{Tr}(\Sigma_k^{-1} S_{i,k})) \quad (27)$$

$$\begin{aligned} Q_2(\Omega) &= \frac{\lambda}{4} \sum_{i,j=1}^N \sum_{k=1}^K \left( (P(s_k|m_i) - P(s_k|m_j)) \right. \\ &\quad \left. (\text{Tr}(\Sigma_k^{-1} S_{j,k}) - \text{Tr}(\Sigma_k^{-1} S_{i,k})) \right) W_{ij} \quad (28) \end{aligned}$$

Similarly, the M-step re-estimation equation for  $\Sigma_k$  can be obtained by taking the derivative of (23) w.r.t.  $\Sigma_k^{-1}$  and setting it to zero:

$$\begin{aligned} \Sigma_k &= \frac{\sum_{i=1}^N P(s_k|m_i) S_{i,k}}{N_k} \quad (29) \\ &\quad - \frac{\lambda \sum_{i,j=1}^N (P(s_k|m_i) - P(s_k|m_j)) (S_{i,k} - S_{j,k}) W_{ij}}{2N_k} \end{aligned}$$

By the regularisation parameter  $\lambda = 0$ , the M-step re-estimation equations (25) and (29) boil down to the M-step in conventional

GMM [44]. As mentioned earlier, the E-step and the M-step is alternated until a termination condition is met. For a detailed derivation of the E-step and the M-step, the readers are kindly referred to [45].

## 5. Performance Evaluation

The classification rate to assess the performance of the proposed methodology was calculated as,

$$C = \frac{CC}{Tot - TU} \times 100 \quad (30)$$

where  $CC$ : vessels which are correctly classified,  $Tot$ : total number of vessels participated in classification process and  $TU$  is number of unclassified vessels i.e. for which votes were tied. In addition, following performance measures were also calculated separately for arterioles ( $a$ ) and venules ( $v$ ) [43],

1. Accuracy;  $= \frac{TP_{a/v} + TN_{a/v}}{TP_{a/v} + TN_{a/v} + FP_{a/v} + FN_{a/v}}$ ,
2. Sensitivity;  $SEN = \frac{TP_{a/v}}{TP_{a/v} + FN_{a/v}}$ ,
3. Specificity;  $SPE = \frac{TN_{a/v}}{TN_{a/v} + FP_{a/v}}$ ,
4. Negative Predicted value;  $NPV = \frac{TN_{a/v}}{TN_{a/v} + FN_{a/v}}$ ,
5. Positive Predicted value;  $PPV = \frac{TP_{a/v}}{TP_{a/v} + FP_{a/v}}$ ,
6. Negative Likelihood Ratio;  $NLR = \frac{1 - Sensitivity}{Specificity}$ ,
7. Positive Likelihood Ratio;  $PLR = \frac{Sensitivity}{1 - Specificity}$ ,

where, TP, FP, TN and FN are True Positive, False Positive, True Negative and False Negative respectively.

## 6. RESULTS

To evaluate the performance of the proposed framework, ground truth was generated by manually grading the retinal vessels into arteriole or venule by two human observers (i.e. Grader 1: an author DR and Grader 2: a clinician). The Grader 1 (DR) was independently and individually trained by clinicians at the *Clinical Research Imaging Centre of the University of Edinburgh, UK* in differentiating the retinal vessels into arteries and veins and has  $\approx 7$  years experience in retinal image analysis.

Grader 1 (DR) did not classify (i.e. labelled as unclassified by grader because of confusing vessels) 19 vessels (i.e. 3.49% of 544 vessels) extracted from images of INSPIRE-AVR dataset while 5.7% of 544 vessels (i.e. 31 vessels) were not classified by Grader 2 due to confusion in determining the label. Moreover, it was noticed that the disparity in labelling the vessels by both the observers were found for only four vessels out of all the vessels which were labelled by two observer.

The classification rate obtained by Grader 1 and Grader 2 on INSPIRE-AVR dataset was 90.65% and 90.83% respectively. The performance measures were computed for Grader 1 w.r.t.

the labels of Grader 2 separately for arterioles and venules and is shown in Table 2. Due to high agreement rate in labelling the vessels by two observer, the classification results on all the datasets were evaluated w.r.t. the Grader 1 (ground truth) in the subsequent paper. Furthermore, the Grader 1 did not classify or grade (because of confusing vessels) 5.87% of 732 vessels and 8.86% of 722 vessels from VICAVER and MESSIDOR dataset respectively (i.e. 43 and 64 vessels respectively).

Table 2: Performance measure (for arterioles and venules separately) of Grader 1 w.r.t Grader 2 when they graded the retinal vessels into arterioles or venules manually on the INSPIRE-AVR dataset.

Performance Measure	arterioles	venules
$SEN$	0.996	0.987
$SPE$	0.987	0.996
$PPV$	0.988	0.995
$NPV$	0.995	0.988
$PLR$	80.36	260.72
$NLR$	0.0038	0.0124

The classification accuracy obtained w.r.t. the ground truth on all datasets using LCGMM (where CLR is the classification rate and UnCL stands for the unclassified vessels) using proposed system is shown in Table 3. Table 3 also shows the results obtained with SMIC [33, 34] and GMM-EM [43] classifier keeping other setting same. Tables 4–6 show the performance measures (evaluated separately for arterioles and venules) with LCGMM, for INSPIRE-AVR, VICAVER and MESSIDOR dataset respectively.

Additional experiment was performed using four features (i.e. Mean of red ( $MR$ ), Mean of Green ( $MG$ ), Mean of Hue ( $MH$ ) and Variance of Red ( $VR$ )) as used in [33, 43] while keeping other setting same. The result obtained is shown in Table 7.

In order to show the effectiveness of the quadrant-pair wise approach the vessel classification was performed without quadrant pairing i.e. all the vessels in the zone B were classified using LCGMM using 3 features ( $MR$ ,  $MG$  and  $VR$ ) as used in this proposed work and 4 features ( $MR$ ,  $MG$ ,  $MH$  and  $VR$ ) as in [33, 43]. The results obtained are mentioned in Table 8.

Table 3: Vessel classification results using LCGMM, GMM-EM and SMIC. Here,  $CLR$  and  $UnCL$  are classification rate and Unclassified vessels percentage respectively

CLASSIFIER		INSPIRE-AVR	VICAVER	MESSIDOR
LCGMM	<b>CLR</b>	90.65%	90.3%	93.8%
	<b>(UnCL)</b>	6.28%	5.8%	3.65%
GMM-EM	<b>CLR</b>	81.26%	76.76%	86%
	<b>(UnCL)</b>	15.6%	24.46%	23%
SMIC	<b>CLR</b>	89.22%	89.95%	93.2%
	<b>(UnCL)</b>	6.3%	6.5%	8.6%

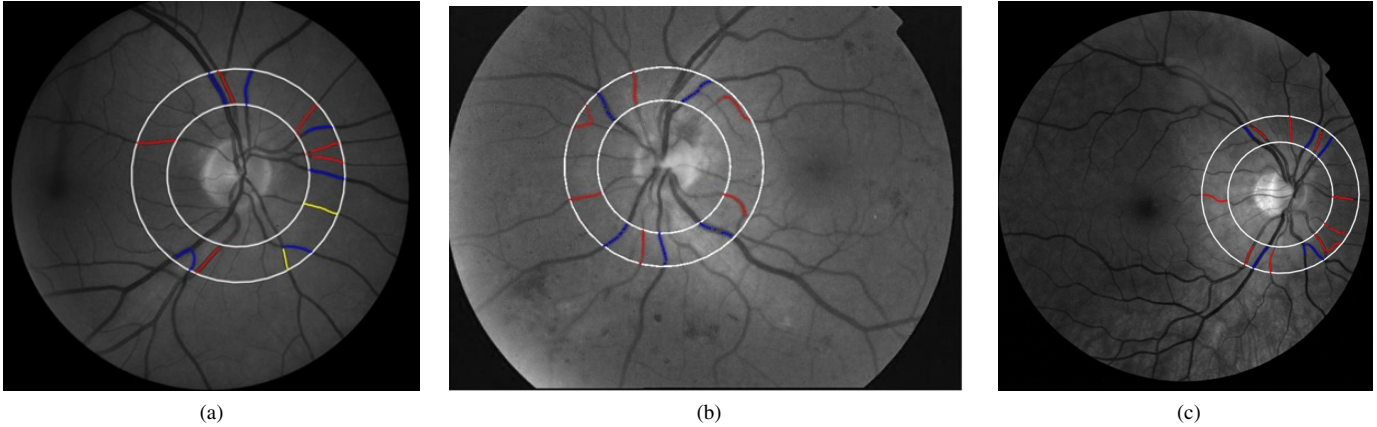


Figure 5: Images showing the classification output on (a) INSPIRE, (b) VICAVR and (c) MESSIDOR image. Vessels in red, blue and yellow shows the system classified arteriole, venule and unclassified vessels respectively

Table 4: Performance measure w.r.t ground truth on INSPIRE-AVR dataset.

Performance Measure	arterioles	venules
<i>SEN</i>	0.946	0.862
<i>SPE</i>	0.862	0.946
<i>PPV</i>	0.885	0.934
<i>NPV</i>	0.934	0.885
<i>PLR</i>	6.83	16.06
<i>NLR</i>	0.062	0.146

Table 5: Performance measure w.r.t ground truth on VICAVR dataset.

Performance Measure	arterioles	venules
<i>SEN</i>	0.907	0.898
<i>SPE</i>	0.898	0.907
<i>PPV</i>	0.915	0.888
<i>NPV</i>	0.888	0.915
<i>PLR</i>	8.89	9.66
<i>NLR</i>	0.104	0.113

Table 6: Performance measure w.r.t ground truth on MESSIDOR dataset.

Performance Measure	arterioles	venules
<i>SEN</i>	0.974	0.895
<i>SPE</i>	0.895	0.973
<i>PPV</i>	0.918	0.966
<i>NPV</i>	0.966	0.918
<i>PLR</i>	9.31	34.32
<i>NLR</i>	0.029	0.107

## 7. DISCUSSION

This proposed methodology classifies the vessels into arteries and veins which is the key part for the calculation of Arterio-Venous Ratio (AVR) (biomarker for various systemic disease).

Table 7: Vessel classification results using LCGMM using 4 features: *MR*, *MG*, *MH* and *VR*. Here, *CLR* and *UnCL* are classification rate and Unclassified vessels percentage respectively

CLASSIFIER		INSPIRE-AVR	VICAVR	MESSIDOR
LCGMM	<b>CLR</b>	85.59%	90.2%	94.0%
	<b>(UnCL)</b>	9.3%	5.2%	2.2%

Table 8: Vessel classification results using LCGMM *without* quadrant pairing using three (*MR*, *MG* and *VR*) and four fixed features (*MR*, *MG*, *MH* and *VR*). Vessel classification results using LCGMM *with* quadrant pairing are also indicated for comparison. Here, *CLR* and *UnCL* are classification rate and Unclassified vessels percentage respectively.

Features	INSPIRE-AVR		VICAVR		MESSIDOR		
	Without	With	Without	With	Without	With	
3 features:	<b>CLR</b>	<b>83.20%</b>	90.65%	<b>85.3%</b>	90.3%	<b>91%</b>	93.8%
	<b>(UnCL)</b>	<b>0%</b>	6.28%	<b>1.16%</b>	5.8%	<b>0.61%</b>	3.65%
4 features:	<b>CLR</b>	<b>81.0%</b>	85.59%	<b>84.8%</b>	90.2%	<b>91.5%</b>	94.0%
	<b>(UnCL)</b>	<b>0.19%</b>	9.3%	<b>1.16%</b>	5.2%	<b>0.3%</b>	2.2%

For the measurement of AVR, it is always advisable to select the good quality vessels which must have a minimum diameter and contrast otherwise it is not possible, even for an ophthalmologist, to distinguish between arteries and veins, especially, when the information about the root of the vessels is not provided [75]. The main aim behind the proposed criterion was to select a combination of medium to wider vessels for classification and for the correct calculation of AVR in future using the proposed framework.

Table 3 presents the comparison of the classification rate obtained using the GMM-EM, SMIC and LCGMM methods. It can be clearly observed that on INSPIRE-AVR, VICAVR and MESSIDOR datasets, the classification rate obtained were 90.65%, 90.3% and 93.8% respectively in zone B using LCGMM. It is observed that classification accuracy obtained with proposed method is higher as compared to methods proposed in [33, 34, 43] (see Table 3). At the same time, it should be note that in [33, 34] the pre-processing method and features used for classification was different as compare to one used in

this paper. Table 7 shows the result obtained using LCGMM when 4 features (i.e. MR, MG, MH and VR) are used, as in [33, 43], while keeping other settings same. It shows that either the classification rate is higher or constant using the proposed system. Comparing the results in Table 3 and 8 shows that the results obtained with quadrant pairing and voting approach are promising compared to without any such approach.

Moreover, the accuracy obtained using the proposed unsupervised methodology is higher in comparison to other reported approaches on same dataset in [20, 27, 31] (see Table 1). The authors in [20] reported vessel classification results on whole image as well as in zone B of INSPIRE-AVR dataset. Their proposed method resulted in different classification rates on the vessels of different calibres. For vessels calibre  $> 5$  pixels, their proposed method gave classification accuracy of 87.9% where as for vessels calibre  $> 20$  pixels it resulted in an accuracy of 97.1% inside the region of interest (ROI) for INSPIRE-AVR dataset. Furthermore, the supervised classification method with feature selection framework of [29] on major vessels of VICAVR dataset yielded only 1% more than that obtained with our proposed method. Moreover, the system of [32] attempted to classify 2 – 4 pixels wide vessels (46% of the total vessels) and vessels with diameter  $\geq 4$  pixels (53% of the total vessel). They tried different supervised approaches and obtained the best classification result with likelihood score propagation (LSP). Their system resulted in the best classification rate (with LSP) of 85.1% and 98.3% respectively. It is important to emphasise here that the methods proposed in [20, 27, 29, 32] are supervised in nature whereas we proposed an unsupervised approach.

In addition, our proposed system also outperforms the previous work where 87.6% [33] and 88.9% [34] classification rate were obtained on the INSPIRE-AVR dataset. Moreover, in the previous experiments [43], the algorithm was tested on ORCADES images of resolution  $2048 \times 3072$  pixels. The method resulted in classification accuracy of 92% on 35 images using GMM-EM algorithm. It should be noted that the direct comparison with the present methodology and [43] is not possible as in the previous work [43] the centerline pixels were extracted by tracking the vessel (which were selected manually) between manually marked points on the vessels whereas in this paper not only the vessels were selected automatically but also the centerline pixels were extracted automatically from segmented vessels. Also, the pre-processing technique and features used for classification was different than that used in this paper. In this proposed system, homomorphic filtering is used for illumination correction before extracting the features whereas in previous work [43], median filtering was used which cannot handle the noise suppression and detail preservation at the same time [87]. Above this, the dataset used for testing the algorithm in the proposed system is different as that of [43]. It should be noted that in the previous work, the extraction of the centerline pixels (i.e. between manually marked points) and the vessel selection was done manually [33, 34], whereas, in the proposed method this procedure is fully automatised.

Additionally, the sensitivity for arterioles and venules was 0.946 and 0.862 respectively (see Table 4). It means that for

the INSPIRE-AVR dataset, the probability of an incorrect classification was only 5.4% and 13.8% for arterioles and venules respectively. Similarly, for the VICAVR and MESSIDOR datasets, the probability of an incorrect classification was (9.3%, 10.2%) and (3%, 11%) for (arterioles, venules) respectively. As seen from Tables 4–6 a high positive likelihood ratio and a low negative likelihood ratio establishes the high reliability of the proposed system.

## 8. CONCLUSION

The categorisation of retinal vessels into arterioles and venules plays a very significant role in the biomarker discovery. In this paper, we proposed a novel unsupervised four step methodology to sort the retinal vessels into two groups - arterioles and venules. The main advantage of the proposed methodology is that it requires no or very less user interaction during each step. Contrary to the usual fact that one needs to always extract a large set of features to obtain a high classification rate, it has been shown that high classification rate can be obtained while utilising only three features in zone B, if a proper preprocessing of the images is performed prior to the final classification. From the results, it can be clearly observed that the LCGMM classifier outperforms the conventional GMM-EM classifier. It is also suggested that for avoiding the false-positives and improving the final classification results, a quadrant-pair wise pooling scheme can be used. The proposed methodology was validated on three different publicly available datasets therefore demonstrates a good potential in computer aided diagnosis and biomarker research.

Although, it has been demonstrated on three different datasets that only three features are sufficient for obtaining the high classification rate but inclusion of other dominant features may potentially improve the performance of the system and it needs to be further investigated. Additionally, there are different factor which are likely to impact the classification performance such as different imaging systems, other retinal zones etc., hence in our future research we aim to tackle such issues.

## References

## References

- [1] H. Leung, J. J. Wang, E. Rojchchina, A. G. Tan, T. Y. Wong, R. Klein, L. D. Hubbard, P. Mitchell, Relationships between age, blood pressure, and retinal vessel diameters in an older population, *Investigative Ophthalmology & Visual Science* 44 (7) (2003) 2900–2904.
- [2] T. Y. Wong, Is retinal photography useful in the measurement of stroke risk?, *Lancet Neurology* 3 (179-183).
- [3] H. Li, W. Hsu, M. L. Lee, T. Y. Wong, Automatic grading of retinal vessel caliber, *IEEE Transactions on Biomedical Engineering* 52 (7) (2005) 1352–1355.
- [4] M. K. Ikram, J. C. Wittman, J. R. Vingerling, M. M. Breteler, A. Hofman, P. T. de Jong, Retinal vessel diameters and risk of hypertension, *hypertension* 47 (2) (2006) 189–194.
- [5] G. Liew, J. J. Wang, P. Mitchell, T. Y. Wong, Retinal vascular imaging: a new tool in microvascular disease research., *Circulation. Cardiovascular imaging* 1 (2) (2008) 156–61, ISSN 1942-0080, doi:\bibinfo{doi}{10.1161/CIRCIMAGING.108.784876}, URL <http://www.ncbi.nlm.nih.gov/pubmed/19808533>.

- [6] F. de Jong, E. Schrijvers, M. Ikram, P. Koudstaal, P. de Jong, A. Hofman, J. Vingerling, M. M. Breteler, Retinal vascular caliber and risk of dementia: the Rotterdam study., *Neurology* 76 (9) (2011) 816–21.
- [7] S. Frost, Y. Kanagasigam, H. Sohrobi, J. Vignarajan, P. Bourgeat, O. Salvado, V. Villemagne, C. C. Rowe, S. L. Macaulay, C. Szoek, et al., Retinal vascular biomarkers for early detection and monitoring of Alzheimers disease, *Translational psychiatry* 3 (2) (2013) e233.
- [8] M. Baker, P.J.Hand, J.J.Wang, T. Wong, Retinal signs and stroke: revisiting the link between the eye and brain., *Stroke* 39 (2008) 1371–1379.
- [9] S. Akbar, M. U. Akram, M. Sharif, A. Tariq, U. ullah Yasin, Arteriovenous ratio and papilledema based hybrid decision support system for detection and grading of hypertensive retinopathy, *Computer methods and programs in biomedicine* 154 (2018) 123–141.
- [10] T. Y. Wong, A. Shankar, R. Klein, B. E. Klein, Retinal vessel diameters and the incidence of gross proteinuria and renal insufficiency in people with type 1 diabetes, *Diabetes* 53 (1) (2004) 179–184.
- [11] F. N. Doubal, T. J.MacGillivray, P. E. Hokke, B. Dhillon, M. S. Dennis, J. M. Wardlaw, Differences in retinal vessels support a distinct vasculopathy causing lacunar stroke., *Neurology* 72 (1773 1778).
- [12] C. Kondermann, D. Kondermann, M. Yan, Blood vessel classification into arteries and veins in retinal images, in: *Medical Imaging, International Society for Optics and Photonics*, 651247–651247, 2007.
- [13] E. Grisan, A. Ruggieri, A divide et impera strategy for automatic classification of retinal vessels into arteries and veins, in: *Engineering in medicine and biology society*, 2003. Proceedings of the 25th annual international conference of the IEEE, vol. 1, IEEE, 890–893, 2003.
- [14] L. Tramontan, E. Grisan, A. Ruggieri, An improved system for the automatic estimation of the Arteriolar-to-Venular diameter Ratio (AVR) in retinal images, in: *Engineering in Medicine and Biology Society*, 2008. EMBS 2008. 30th Annual International Conference of the IEEE, IEEE, 3550–3553, 2008.
- [15] M. Saez, S. González-Vázquez, M. González-Penedo, M. A. Barceló, M. Pena-Seijo, G. C. de Tuero, A. Pose-Reino, Development of an automated system to classify retinal vessels into arteries and veins, *Computer methods and programs in biomedicine* 108 (1) (2012) 367–376.
- [16] V. S. Joshi, M. K. Garvin, J. M. Reinhardt, M. D. Abramoff, Automated artery-venous classification of retinal blood vessels based on structural mapping method, *Proc. SPIE Medical Imaging, Computer-Aided Diagnosis* 8315 (2012) 83150I.
- [17] Q. Mirsharif, F. Tajeripour, H. Pourreza, Automated characterization of blood vessels as arteries and veins in retinal images, *Computerized Medical Imaging and Graphics* 37 (7) (2013) 607–617.
- [18] M. Niemeijer, B. van Ginneken, M. D. Abramoff, Automatic classification of retinal vessels into arteries and veins, in: *SPIE medical imaging, International Society for Optics and Photonics*, 72601F–72601F, 2009.
- [19] C. Muramatsu, Y. Hatanaka, T. Iwase, T. Hara, H. Fujita, Automated selection of major arteries and veins for measurement of arteriolar-to-venular diameter ratio on retinal fundus images, *Computerized Medical Imaging and Graphics* 35 (6) (2011) 472–480.
- [20] B. Dashtbozorg, A. M. Mendonça, A. Campilho, An automatic graph-based approach for artery/vein classification in retinal images, *IEEE Transactions on Image Processing* 23 (3) (2014) 1073–1083.
- [21] X. Xu, W. Ding, M. D. Abramoff, R. Cao, An improved arteriovenous classification method for the early diagnostics of various diseases in retinal image, *Computer Methods and Programs in Biomedicine* 141 (2017) 3–9.
- [22] F. Huang, B. Dashtbozorg, T. Tan, B. M. ter Haar Romeny, Retinal artery/vein classification using genetic-search feature selection, *Computer methods and programs in biomedicine* 161 (2018) 197–207.
- [23] K. Rothaus, X. Jiang, P. Rhiem, Separation of the retinal vascular graph in arteries and veins based upon structural knowledge, *Image and Vision Computing* 27 (7) (2009) 864–875, ISSN 02628856, doi:\bibinfo{doi}{10.1016/j.imavis.2008.02.013}, URL <http://linkinghub.elsevier.com/retrieve/pii/S0262885608000590>.
- [24] Q. Hu, M. D. Abramoff, M. K. Garvin, Automated separation of binary overlapping trees in low-contrast color retinal images, in: *International Conference on Medical Image Computing and Computer-Assisted Intervention*, Springer, 436–443, 2013.
- [25] R. Estrada, M. J. Allingham, P. S. Mettu, S. W. Cousins, C. Tomasi, S. Farsiu, Retinal artery-vein classification via topology estimation, *IEEE transactions on medical imaging* 34 (12) (2015) 2518–2534.
- [26] M. D. Abramoff, M. K. Garvin, M. Sonka, Retinal imaging and image analysis, *IEEE reviews in biomedical engineering* 3 (2010) 169–208.
- [27] M. Niemeijer, X. Xu, A. V. Dumitrescu, P. Gupta, B. van Ginneken, J. C. Folk, M. D. Abramoff, Automated measurement of the arteriolar-to-venular width ratio in digital color fundus photographs, *IEEE Transactions on medical imaging* 30 (11) (2011) 1941–1950.
- [28] A. Zamperini, A. Giachetti, Effective features for artery-vein classification in digital fundus images, 25th International Symposium on Computer-Based Medical Systems (CBMS) URL [http://ieeexplore.ieee.org/xpls/abs\\_all.jsp?arnumber=6266336](http://ieeexplore.ieee.org/xpls/abs_all.jsp?arnumber=6266336).
- [29] V. Vijayakumar, D. D. Koozekanani, R. White, J. Kohler, S. Roychowdhury, K. K. Parhi, Artery/vein classification of retinal blood vessels using feature selection, in: *Engineering in Medicine and Biology Society (EMBC), 2016 IEEE 38th Annual International Conference of the IEEE*, 1320–1323, 2016.
- [30] N. Hatami, M. Goldbaum, Automatic Identification of Retinal Arteries and Veins in Fundus Images using Local Binary Patterns, arXiv preprint arXiv:1605.00763 .
- [31] S. Vázquez, B. Cancela, N. Barreira, M. G. Penedo, M. Rodríguez-Blanco, M. P. Seijo, G. C. de Tuero, M. A. Barceló, M. Saez, Improving retinal artery and vein classification by means of a minimal path approach, *Machine Vision and Applications* 24 (5) (2013) 919–930.
- [32] F. Girarda, C. Kavalech, F. Cherieta, Joint segmentation and classification of retinal arteries/veins from fundus images, *Artificial Intelligence in Medicine* 94 (2019) 96–109.
- [33] D. Relan, L. Ballerini, E. Trucco, T. MacGillivray, Retinal Vessel Classification Based on Maximization of Squared-Loss Mutual Information, in: *Machine Intelligence and Signal Processing*, Springer, 77–84, 2016.
- [34] D. Relan, R. Relan, Multiscale self-quotient filtering for an improved unsupervised retinal blood vessels characterisation, *Biomedical engineering letters* 8 (1) (2018) 59–68.
- [35] R. Welikala, P. Foster, P. Whincup, A. R. Rudnicka, C. G. Owen, D. Strachan, S. Barman, et al., Automated arteriole and venule classification using deep learning for retinal images from the UK Biobank cohort, *Computers in biology and medicine* 90 (2017) 23–32.
- [36] J. Y. Choi, T. K. Yoo, J. G. Seo, J. Kwak, T. T. Um, T. H. Rim, Multi-categorical deep learning neural network to classify retinal images: a pilot study employing small database, *PloS one* 12 (11) (2017) e0187336.
- [37] B. K. Trivijoyo, W. Budiharto, E. Abdurachman, The Classification of Hypertensive Retinopathy using Convolutional Neural Network, *Procedia Computer Science* 116 (2017) 166–173.
- [38] Z. Yan, X. Yang, K.-T. T. Cheng, A Three-stage Deep Learning Model for Accurate Retinal Vessel Segmentation, *IEEE journal of biomedical and health informatics* .
- [39] M. I. Meyer, A. Galdran, P. Costa, A. M. Mendonça, A. Campilho, Deep Convolutional Artery/Vein Classification of Retinal Vessels, in: *International Conference Image Analysis and Recognition*, Springer, 622–630, 2018.
- [40] G. Tetteh, V. Efremov, N. D. Forkert, M. Schneider, J. Kirschke, B. Weber, C. Zimmer, M. Piraud, B. H. Menze, DeepVesselNet: Vessel Segmentation, Centerline Prediction, and Bifurcation Detection in 3-D Angiographic Volumes, arXiv preprint arXiv:1803.09340 .
- [41] M. Li, Q. Yin, M. Lu, Retinal Blood Vessel Segmentation Based on Multi-Scale Deep Learning, in: *2018 Federated Conference on Computer Science and Information Systems (FedCSIS)*, IEEE, 1–7, 2018.
- [42] H. Zhao, Y. Sun, H. Li, Retinal vascular junction detection and classification via deep neural networks, *Computer Methods and Programs in Biomedicine* 183 (2020) 105096, ISSN 0169-2607, URL <http://www.sciencedirect.com/science/article/pii/S016926071930940X>.
- [43] D. Relan, T. MacGillivray, L. Ballerini, E. Trucco, Retinal vessel classification: sorting arteries and veins, in: *Engineering in Medicine and Biology Society (EMBC), 2013 35th Annual International Conference of the IEEE, IEEE*, 7396–7399, 2013.
- [44] C. M. Bishop, *Pattern Recognition and Machine Learning*, Springer .
- [45] J. Liu, D. Cai, X. He, Gaussian mixture model with local consistency, in: *Twenty-Fourth AAAI Conference on Artificial Intelligence*, 2010.
- [46] I. Pitas, A. N. Venetsanopoulos, *Homomorphic Filters*, Springer US, Boston, MA, ISBN 978-1-4757-6017-0, 217–243, doi:\bibinfo{doi}{10.1007/978-1-4757-6017-0\_7}, URL [http://dx.doi.org/10.1007/978-1-4757-6017-0\\_7](http://dx.doi.org/10.1007/978-1-4757-6017-0_7), 1990.

- [47] V. I. Ponomarev, O. B. Pogrebnyak, Image enhancement by homomorphic filters, doi:\binfo{doi}[10.1117/12.217396], URL <http://dx.doi.org/10.1117/12.217396>, 1995.
- [48] E. Ricci, R. Perfetti, Retinal blood vessel segmentation using line operators and support vector classification, *IEEE transactions on medical imaging* 26 (10) (2007) 1357–1365.
- [49] R. Kharghanian, A. Ahmadyard, Retinal blood vessel segmentation using gabor wavelet and line operator, *International Journal of Machine Learning and Computing* 2 (5) (2012) 593.
- [50] U. T. Nguyen, A. Bhuiyan, L. A. Park, K. Ramamohanarao, An effective retinal blood vessel segmentation method using multi-scale line detection, *Pattern recognition* 46 (3) (2013) 703–715.
- [51] J. Canny, A computational approach to edge detection, *IEEE Transactions on pattern analysis and machine intelligence* (6) (1986) 679–698.
- [52] N. Roy, V. Jain, Additive and Multiplicative Noise Removal by using Gradient Histogram Preservations Approach, *International Journal of Computer Applications* 130 (2) (2015) 11–16.
- [53] A. Makandar, D. Mulmani, M. Jevoor, Comparative Study of Different Noise Models and Effective Filtering Techniques, *International Journal of Science and Research (IJSR)* 3 (8) (2014) 458–464.
- [54] K. Delac, M. Grgic, T. Kos, Sub-image homomorphic filtering technique for improving facial identification under difficult illumination conditions, in: *International Conference on Systems, Signals and Image Processing*, vol. 1, 21–23, 2006.
- [55] I. Stainvas, D. Lowe, A generative model for separating illumination and reflectance from images, *Journal of Machine Learning Research* 4 (Dec) (2003) 1499–1519.
- [56] A. P. A. H. Abbas, J. Harbi, Image Enhancement By Using Homomorphic Filtering Model, in: *The 1st International Conference on Information Technology (ICoIT'17)*, 335, 2017.
- [57] S. A. M. Saleh, H. Ibrahim, Mathematical equations for homomorphic filtering in frequency domain: a literature survey, in: *Proceedings of the International Conference on Information and Knowledge Management*, 74–77, 2012.
- [58] A. V. Stanton, B. Wasan, A. Cerutti, S. Ford, R. Marsh, P. P. Sever, S. A. Thom, A. D. Hughes, Vascular network changes in the retina with age and hypertension., *Journal of hypertension* 13 (12 Pt 2) (1995) 1724–1728.
- [59] T. Y. Wong, R. McIntosh, Hypertensive retinopathy signs as risk indicators of cardiovascular morbidity and mortality, *British medical bulletin* 73 (1) (2005) 57–70.
- [60] G. Liew, J. J. Wang, Retinal vascular signs: a window to the heart?, *Revista Española de Cardiología (English Edition)* 64 (6) (2011) 515–521.
- [61] A. Ishibazawa, T. Nagaoka, H. Yokota, A. Takahashi, T. Omae, Y.-S. Song, T. Takahashi, A. Yoshida, Characteristics of retinal neovascularization in proliferative diabetic retinopathy imaged by optical coherence tomography angiography, *Investigative ophthalmology & visual science* 57 (14) (2016) 6247–6255.
- [62] A. D. Proia, M. C. Caldwell, Intraretinal neovascularization in diabetic retinopathy, *Archives of ophthalmology* 128 (1) (2010) 142–144.
- [63] T. Y. Wong, R. Klein, D. J. Couper, L. S. Cooper, E. Shahar, L. D. Hubbard, M. R. Wofford, A. R. Sharrett, Retinal microvascular abnormalities and incident stroke: the Atherosclerosis Risk in Communities Study, *The Lancet* 358 (9288) (2001) 1134–1140.
- [64] M. L. Baker, P. J. Hand, J. J. Wang, T. Y. Wong, Retinal signs and stroke: revisiting the link between the eye and brain, *Stroke* 39 (4) (2008) 1371–1379.
- [65] P. K. Roy, U. T. Nguyen, A. Bhuiyan, K. Ramamohanarao, An effective automated system for grading severity of retinal arteriovenous nicking in colour retinal images, in: *Engineering in Medicine and Biology Society (EMBC), 2014 36th Annual International Conference of the IEEE, IEEE*, 6324–6327, 2014.
- [66] Y. Guo, Ü. Budak, A. Şengür, A novel retinal vessel detection approach based on multiple deep convolution neural networks, *Computer methods and programs in biomedicine* 167 (2018) 43–48.
- [67] L. Zhou, Q. Yu, X. Xu, Y. Gu, J. Yang, Improving dense conditional random field for retinal vessel segmentation by discriminative feature learning and thin-vessel enhancement, *Computer methods and programs in biomedicine* 148 (2017) 13–25.
- [68] K. J. Noh, S. J. Park, S. Lee, Scale-Space Approximated Convolutional Neural Networks for Retinal Vessel Segmentation, *Computer Methods and Programs in Biomedicine* .
- [69] M. M. Fraz, P. Remagnino, A. Hoppe, B. Uyyanonvara, A. R. Rudnicka, C. G. Owen, S. A. Barman, Blood vessel segmentation methodologies in retinal images—a survey, *Computer methods and programs in biomedicine* 108 (1) (2012) 407–433.
- [70] S. Moccia, E. De Momi, S. El Hadji, L. S. Mattos, Blood vessel segmentation algorithms Review of methods, datasets and evaluation metrics, *Computer methods and programs in biomedicine* 158 (2018) 71–91.
- [71] C.-C. Chang, C.-C. Lin, P.-Y. Pai, Y.-C. Chen, A novel retinal blood vessel segmentation method based on line operator and edge detector, in: *Intelligent Information Hiding and Multimedia Signal Processing, 2009. IHH-MSP'09. Fifth International Conference on, IEEE*, 299–302, 2009.
- [72] V. M. Saffarzadeh, A. Osareh, B. Shadgar, Vessel segmentation in retinal images using multi-scale line operator and K-means clustering, *Journal of medical signals and sensors* 4 (2) (2014) 122.
- [73] L. Lam, S. Lee, C. Suen, Thinning methodologies - a comprehensive survey, *IEEE TPAMI* 14 (1992.) 869–885.
- [74] MATLAB code for finding junctions, <http://www.peterkovesi.com/matlabfns/LineSegments/findendsjunctions.m>, ????
- [75] R. Chrastek, et al., Automated Calculation of Retinal Arterio-Venous Ratio, *Investigative Ophthalmology Visual Science* 44 (2003) 3106.
- [76] S. Vazquez, B. Cancela, N. Barreira, M. G. Penedo, M. Saez, On the automatic computation of the arterio-venous ratio in retinal images: Using minimal paths for the artery/vein classification, in: *Digital Image Computing: Techniques and Applications (DICTA), 2010 International Conference on, IEEE*, 599–604, 2010.
- [77] H. Jelinek, C. Depardieu, C. Lucas, D. Cornforth, W. Huang, M. Cree, et al., Towards vessel characterization in the vicinity of the optic disc in digital retinal images (2005) 2–7.
- [78] S. T. Roweis, L. K. Saul, Nonlinear dimensionality reduction by locally linear embedding, *science* 290 (5500) (2000) 2323–2326.
- [79] J. B. Tenenbaum, V. De Silva, J. C. Langford, A global geometric framework for nonlinear dimensionality reduction, *science* 290 (5500) (2000) 2319–2323.
- [80] A. P. Dempster, N. M. Laird, D. B. Rubin, Maximum likelihood from incomplete data via the EM algorithm, *Journal of the Royal Statistical Society: Series B (Methodological)* 39 (1) (1977) 1–22.
- [81] M. Belkin, P. Niyogi, V. Sindhwani, Manifold regularization: A geometric framework for learning from labeled and unlabeled examples, *Journal of machine learning research* 7 (Nov) (2006) 2399–2434.
- [82] D. Cai, X. Wang, X. He, Probabilistic dyadic data analysis with local and global consistency, in: *Proceedings of the 26th annual international conference on machine learning, ACM*, 105–112, 2009.
- [83] D. Zhou, O. Bousquet, T. N. Lal, J. Weston, B. Schölkopf, Learning with local and global consistency, in: *Advances in neural information processing systems*, 321–328, 2004.
- [84] X. Zhu, J. Lafferty, Harmonic mixtures: combining mixture models and graph-based methods for inductive and scalable semi-supervised learning, in: *Proceedings of the 22nd international conference on Machine learning, ACM*, 1052–1059, 2005.
- [85] M. Belkin, P. Niyogi, Laplacian Eigenmaps and Spectral Techniques for Embedding and Clustering, *Advances in Neural Information Processing Systems* 14.
- [86] F. Chung, F. Graham, A. M. Society, C. C. on Recent Advances in Spectral Graph Theory, C. B. of the Mathematical Sciences, *Spectral Graph Theory, CBMS Regional Conference Series, American Mathematical Society, ISBN 9780821803158*, 1997.
- [87] E. R. Davies, *Machine vision: theory, algorithms, practicalities*, Elsevier, 2004.

**Declaration of Competing Interest**

This is to declare that the authors no conflict of interest to declare. This statement is also to certify that all authors have seen and approved the manuscript being submitted. We warrant that the article is the authors' original work. We warrant that the article has not received prior publication and is not under consideration for publication elsewhere. On behalf of all co-authors, the corresponding author shall bear full responsibility for the submission.

This research has not been submitted for publication nor has it been published in whole or in part elsewhere. We attest to the fact that all authors listed on the title page have contributed significantly to the work, have read the manuscript, attest to the validity and legitimacy of the data and its interpretation, and agree to its submission to the Journal of Computer Methods and Programs in Biomedicine.

Journal Pre-proof